Contents lists available at ScienceDirect

Nuclear Medicine and Biology

journal homepage: www.elsevier.com/locate/nucmedbio

Target engagement of an anti-MT1-MMP antibody for triple-negative breast cancer PET imaging and beta therapy☆

Natalia Magro [a], Marta Oteo [a], Eduardo Romero [a], Marta Ibáñez-Moragues [a],
Victor Manuel Lujan [a], Laura Martínez [a], Oscar Vela [a], Maria Elena López-Melero [b],
Alicia G. Arroyo [c], Guillermo Garaulet [d], Jorge Luis Martínez-Torrecuadrada [e],
Francisca Mulero [d,*], Miguel Angel Morcillo [a,**]

[a] Medical Applications of Ionizing Radiations Unit, Centro de Investigaciones Energéticas, Medioambientales y Tecnológicas (CIEMAT), Madrid, Spain
[b] Department of Atomic, Molecular, and Nuclear Physics, University of Granada, Spain
[c] Centro de Investigaciones Biológicas Margarita Salas (CIB-CSIC), Madrid, Spain
[d] Molecular Imaging Unit, Spanish National Cancer Research Center (CNIO), Madrid, Spain
[e] Protein Production Unit, Spanish National Cancer Research Center (CNIO), Madrid, Spain

ARTICLE INFO

ABSTRACT

Purpose: Triple-negative breast cancer (TNBC) is a highly aggressive subtype of breast cancer that lacks effective diagnostic and therapeutic options. Membrane type 1 matrix metalloproteinase (MT1-MMP) is an attractive biomarker for improving patient selection. This study aimed to develop a theranostic tool using a highly tumour-selective anti-MT1-MMP antibody (LEM2/15) radiolabelled with ^{89}Zr for PET and ^{177}Lu for therapy in a TNBC murine model.

Methods: The LEM2/15 antibody and IgG isotype control were radiolabelled with ^{89}Zr. PET imaging was performed in a TNBC orthotopic mouse model at 1, 2, 4, and 7 days after administration. Tissue biodistribution and pharmacokinetic parameters were analysed and Patlak linearisation was used to calculate the influx rate of irreversible uptake. The TNBC mice were treated with [^{177}Lu]Lu-DOTA-LEM2/15 (single- or 3-dose regimen) or saline. Efficacy of [^{177}Lu]Lu-DOTA-LEM2/15 was evaluated as tumour growth and DNA damage (γH2AX) in MDA 231-BrM2-831 tumours.

Results: At 7 days post-injection, PET uptake in tumour xenografts revealed a 1.6-fold and 2.4-fold higher tumour-to-blood ratio for [^{89}Zr]Zr-Df-LEM2/15 in the non-blocked group compared to the blocked and IgG isotype control groups, respectively. Specific uptake of LEM2/15 in TBNC tumours mediated by MT1-MMP-binding was demonstrated by the Patlak linearisation method, providing insights into the potential efficacy of LEM2/15-based treatments. A similar uptake was found for [^{89}Zr]Zr-Df-LEM2/15 and [^{177}Lu]Lu-DOTA-LEM2/15 in tumours 7 days post-injection (6.80 ± 1.31 vs. 5.61 ± 0.66 %ID/g). Tumour doubling time was longer in the [^{177}Lu]Lu-DOTA-LEM2/15 3-dose regimen treated group compared to the control (50 vs. 17 days, respectively). The percentage of cells with γH2AX-foci was higher in tumours treated with [^{177}Lu]Lu-DOTA-LEM2/15 3-dose regimen compared to tumours non-treated or treated with [^{177}Lu]Lu-DOTA-LEM2/15 single-dose (12 % vs. 4–5 %).

Conclusions: The results showed that the ^{89}Zr/^{177}Lu-labelled anti-MT1-MMP mAb (LEM2/15) pair facilitated immune-PET imaging and reduced tumour growth in a preclinical TNBC xenograft model.

---

1. Introduction

Breast cancer is the most commonly diagnosed cancer and the leading cause of death in females. According to the 2020 GLOBOCAN, approximately 2.3 million (11.7 %) new cases were diagnosed, and there were 684,996 (6.9 %) deaths worldwide. At the molecular level, breast cancer is a heterogeneous disease comprising several molecular subtypes, based on the presence or absence of molecular markers. Triple-negative breast cancer (TNBC) accounts for 10–20 % of breast cancer cases and lacks the expression of the oestrogen receptor (ER), progesterone receptor (PR), and human epidermal growth factor receptor 2 (HER2) [1]. TNBCs are a heterogeneous group of tumours that display a more aggressive phenotype with worse survival rates due to a greater number of them becoming metastatic compared to other subtypes [2]. Currently, targeted therapy is not performed as a standard of care, relying exclusively on cytotoxic chemotherapy [3–5]. In clinical practice, breast cancer diagnosis relies on mammography, breast MRI, ultrasonography, biopsy, and molecular imaging. However, precision medicine for breast cancer has traditionally been based on the results of tissue sampling of the primary breast tumour and metastatic sites, which is an invasive process. Immunohistochemical analysis of the biopsied material is not representative of the entire tumour because tumours are known to be highly heterogeneous, evolve over time, and their biomarker status can differ from the primary tumour to metastatic lesions [6,7].

Overexpression of several druggable target receptors for TNBC has recently been discovered. A few monoclonal antibodies have been approved for clinical use in metastatic or refractory TNBC, such as PARP inhibitors, anti-PD-L1 antibodies, and antibody-drug conjugates [8]. Numerous therapeutic targets have been investigated for TNBC treatment. The development of new non-invasive imaging agents to help select patients most likely to benefit from these treatments was prompted by the availability of new treatments directed toward these targets. A good candidate biomarker to enhance TNBC noninvasive detection and subsequent patient management would be membrane type 1 matrix metalloproteinase (MT1-MMP or MMP14), a surface-bound MMP overexpressed in many tumours, including TNBC, associated with poor prognosis and potentially important in lung and brain metastasis of breast cancer [9–11]. It acts as a protease for extracellular matrix (ECM) biomolecules such as collagen, which subsequently activates cell signalling pathways and enables cell invasion through ECM [12]. MT1-MMP expression levels can be monitored in real-time using immuno-PET, a noninvasive imaging technique that combines the high sensitivity and quantitative capabilities of PET with the specificity and selectivity of antibodies [13]. This information can be used to determine whether a patient will benefit from targeted therapy. Additionally, PET scans performed during therapy might be useful for quick assessment of the state of the patient's condition early in the course of treatment. Zirconium-89 (^{89}Zr, $T_{1/2}$:78.4 h, E_{mean}: 385 KeV) emerges as an ideal radionuclide for immuno-PET due to its fitting emission energy properties and long half-life, which matches the circulation half-life of monoclonal antibodies (mAbs, typically 2–4 days), enabling plenty of time for tumour and organ marker screening in vivo [14,15]. In vivo analysis of the interaction of antibodies with their target biomolecules (target engagement) is possible using immuno-PET with ^{89}Zr-labelled antibodies. The Patlak linearisation applied to the ^{89}Zr-immuno-PET quantification data can be used to estimate the reversible and irreversible uptake of ^{89}Zr-labelled mAb in the tumour based on graphical analysis of multiple-time tissue uptake data [16,17].

Theranostics is based on a combination of diagnostic imaging and therapy. To incorporate cytotoxic payloads into targeting agents, two strategies are to conjugate nonspecific cytotoxic drugs and attach radioisotopes that result in DNA strand breaks (Targeted Radionuclide Therapy or TRT). Typically, peptides and antibodies are used as targeting agents because they can be chemically modified with cytotoxic payloads while retaining their pharmacokinetic properties and specific

binding to target proteins on cancer cell surfaces. Once bound to the target protein, these vehicles can be internalised into cancer cells and deliver their cytotoxic payload. Radiolabelled monoclonal antibodies, in conjunction with imaging methods such as PET or SPECT, provide vital information on pharmacokinetics, pharmacodynamics, antigen expression heterogeneity, and dynamic changes in tumours [18]. Thus, innovative strategies that combine targeting, diagnosis, and therapeutics are essential for addressing the current challenges in TNBC treatment. There are three types of radiation related to TRT: β-particles, α-particles, and Auger electrons, which can irradiate volumes with multicellular, cellular, and subcellular dimensions, respectively [19]. β-emitters are considered ideal for targeting large tumours because of their long-range path length and ability to induce the formation of radical species that are damaging to DNA [20]. Among these, ^{177}Lu ($T_{1/2}$ = 6.73 days) is a low-energy β-emitter (0.497 MeVmax) with a tissue penetration of up to 1.6 mm, which has been successfully used in preclinical studies and several clinical trials.

With this aim, we explored a theranostics approach utilising an antibody (LEM2/15) against the catalytic domain of MT1-MMP and a pair of radioligands labelled with diagnostic (^{89}Zr) and therapeutic (^{177}Lu) radionuclides. PET imaging with [^{89}Zr]Zr-Df-LEM2/15 would include confirmation of the presence of MT1-MMP in the tumour and possible metastases (diagnosis) before [^{177}Lu]Lu-DOTA-LEM2/15 targeted radionuclide therapy (TRT) of individuals with tumours expressing MT1-MMP. ^{89}Zr is used as a PET imaging nuclide, whereas ^{177}Lu has become a key therapeutic radionuclide of choice for TRT because of its ability to deliver radiation within the tumour rather than in the healthy surrounding tissue and its relatively long physical half-life that allows optimal tumour accumulation for effective TRT [21]. Therefore, we developed a theranostic tool with [^{89}Zr]Zr-Df-LEM2/15 as an imaging marker and [^{177}Lu]Lu-DOTA-LEM2/15 as a therapeutic agent to specifically target MT1-MMP expression in a TNBC xenograft model.

2. Materials and methods

2.1. LEM2/15 radiolabeling with ^{89}Zr

The bifunctional chelator *p*-SCN-Bn-Deferoxamine (Df) (Macrocyclics, Dallas, TX) was conjugated to the anti-MT1-MMP monoclonal antibody LEM2/15 and IgG1 isotype control (Mouse IgG1,κ clone MOPC-21, BioXCell, Lebanon, NH, USA), and subsequent ^{89}Zr radiolabeling was performed by adaptation of published protocols [22,23]. ^{89}Zr (~2.7 GBq/mL supplied in 1 M oxalic acid) was obtained from BV Cyclotron VU (Amsterdam, the Netherlands).

For conjugation, 2 mg of antibody in 1 mL of solution at pH 8.9–9.1, adjusted with 0.1 M Na$_2$CO$_3$ (maximum of 0.1 mL), were mixed with the bifunctional chelator dissolved in DMSO at a final concentration of 3.5 mM and at a molar ratio of 1:5. The reaction mixture was incubated at 37 °C for 90 min at 550 rpm using a Thermomixer (Eppendorf, Hamburg, Germany). The non-conjugated chelator was removed using a PD-10 desalting column (Cytiva, Uppsala, Sweden) using 5 mg/mL gentisic acid in 0.25 M sodium acetate trihydrate (pH 5.4–5.6) as the eluent.

For radiolabelling of Df-LEM2/15 and Df-IgG1 isotype control, the volume of ^{89}Zr-oxalic acid solution corresponding to 62.5 MBq was adjusted to a total volume of 200 μL using 1 M oxalic acid. Next, 90 μL of 2 M Na$_2$CO$_3$ was added, and the mixture was incubated for 3 min at room temperature. Then, 1 mL of 0.5 M HEPES and 710 μL of Df-LEM2/15 or Df-IgG (1 mg/mL) were added. The pH was checked to be 6.8–7.2 using pH indicator strips (Merck, Darmstadt, Germany). After 60 min of incubation at 37 °C using a Thermomixer (Eppendorf, Hamburg, Germany), the mixture was eluted through a previously equilibrated PD-10 desalting column (Cytiva, Uppsala, Sweden) with phosphate-buffered saline (PBS) (Gibco, Waltham, MA, USA). One aliquot (2 mL) was collected and counted in an IBC dose calibrator (Comercer, Castel Bolognese, RA, Italy) corresponding to the peak activity fraction.

2.1.1. Quality control - HPLC

An aliquot of [^{89}Zr]Zr-Df-IgG and [^{89}Zr]Zr-Df-LEM2/15 was taken to analyse the radiochemical purity (RQP) by radio-HPLC in a Jasco HPLC system equipped with a photodiode array UV-detector MD-4015 (Jasco, Easton, MD), a radioactivity detector LB 500 HERM (Berthold, Bad Wildbad, Germany), and a gel filtration chromatography BioSep Sec-s2000 145 Å LC Column (5 μm, 300 × 7.8 mm).

2.1.2. Quality control - ELISA

Nunc-Immuno 96-well plates (Thermo Fischer Scientific, Roskilde, Denmark) were coated overnight at 4 °C with MT1-MMP catalytic site (CAT-MT1-MMP, CNIO Protein Production Unit [24]) or an irrelevant recombinant protein as a negative control (0.3 μg/well). The wells were washed with PBS, and serial dilutions of LEM2/15, conjugated LEM2/15, and [^{89}Zr]Zr-Df-LEM2/15 in blocking buffer (5 % skim milk powder in 0.05 % Tween 20) were added and incubated for 30 min at room temperature. The wells were then washed with PBS containing Tween 0.05 % and incubated at room temperature for 30 min with HRP-labelled anti-mouse IgG (Sigma-Aldrich, Saint Louis, MO, USA). Finally, 3,3′,5,5′-tetramethylbenzidinde (TMB) (Sigma-Aldrich, Saint Louis, MO, USA) was used as the substrate. The reaction was stopped by adding 100 μL of 1 M sulfuric acid (Sigma-Aldrich, Saint Louis, MO, USA) and the OD450 was measured using a Fluostar Omega plate reader (BMG Labtech, Ortenberg, Germany).

2.1.3. Quality control - determination of the immunoreactive fraction (IRF)

Nunc-Immuno 96-well plates (Thermo Fischer Scientific, Roskilde, Denmark) were coated with 10 serial 1/2 dilutions of CAT-MT1-MMP (0.3–0.00029 μg/well). The volume in each well was made up to 100 μL using PBS. The microplate was incubated overnight at 4 °C and covered. The next day, the coating solution was removed, and the coated wells were rinsed three times with 200 μL PBS (1×) and blocked with 200 μL of blocking buffer for 2 h (5 % skimmed milk powder in PBS containing 0.05 % Tween 20). Then, the blocking buffer was removed and the labelled antibody was added to a final concentration of 0.6 ng/μL in a final volume of 50 μL per well (30 ng/well). The microplate was incubated for 30 min at 4 °C, after which the supernatant was discarded and the wells were rinsed twice with PBS-Tween 0.05 %. Next, 200 μL of NaOH 1 M was added to the washed wells to recover bound radiolabelled antibodies, the solution was transferred to scintillation tubes, and the amount of radioactivity bound to the individual wells was determined by gamma scintillation counting. The IRF was determined from a plot of total radioactivity applied/radioactivity bound (T/B) versus the inverse of the concentration of CAT-MT1-MMP, according to Lindmo et al. [25]. In this plot, the IRF is the inverse of the intercept on the ordinate (1/Y). To determine the amount of non-specific binding to the wells, a well which had been coated with a non-specific antigen (irrelevant recombinant protein) was subjected to the same conditions as described above, and the amount of radiolabelled antibodies bound to the well was measured.

2.2. LEM2/15 radiolabeling with ^{177}Lu

The commercial bifunctional chelating agent DOTA-NHS (2,2′,2″-(10-(2-((2,5-dioxopyrrolidin-1-yl)oxy)-2-oxoethyl)-1,4,7,10-tetraazacyclododecane-1,4,7-triyl)triacetic acid) was purchased from CheMatech (Dijon, France). A 20-fold molar excess of DOTA-NHS was dissolved in 20 μL of DMSO and slowly added to LEM2/15 (2.1 mg, 1 mL). The pH was adjusted with sodium carbonate 0.1 M to 8.5. Then, the mixture was incubated at 37 °C for 3 h and 550 rpm using a Thermomixer (Eppendorf, Hamburg, Germany). No-carrier-added ^{177}LuCl$_3$ was obtained from Curium Pharma Spain (Madrid, Spain).

^{177}LuCl$_3$ (in 0.04 M HCl) was diluted with HCl (0.04 M) to a total volume of 150 μL and subsequently 300 MBq ^{177}Lu was added to 1 mL (1 mg) DOTA-LEM2/15 conjugated solution (final pH = 5.5). The mixture was incubated at 37 °C for 3 h and 550 rpm using a Thermomixer (Eppendorf, Hamburg, Germany), then 50 μL of EDTA 0.05 M was added to the sample for 15 min at room temperature to bind with free ^{177}Lu. The reaction mixture was transferred on a PD-10 desalting column (Cytiva, Uppsala, Sweden) equilibrated by passing 40 mL of PBS to exchange the buffer to PBS and to remove the unreacted ^{177}Lu. Finally, the [^{177}Lu]Lu-DOTA-LEM2/15 was collected in 2 mL.

Radiochemical yield, radiochemical purity and the affinity against the CAT-MT1-MMP of the radiolabelled conjugated were determined under the same conditions as described above.

2.3. Cell lines

The MDA 231-BrM–831 breast cancer cell line, established from the MDA-MB-231 cell line, was generously provided by Dr. Joan Massagué, Memorial Sloan Kettering Cancer Center (NY, USA). The cells were cultured according to standard mammalian tissue culture protocols in Dulbecco's Modified Eagle's Medium + GlutaMax (Gibco, Waltham, MA, USA) supplemented with 10 % foetal bovine serum (FBS) (Gibco, Waltham, MA, USA) and 100 units/mL penicillin/100 μg/mL streptomycin (Gibco, Waltham, MA, USA) at 37 °C in a humidified atmosphere with 5 % CO$_2$.

2.4. Animal model

All animals involved in the experiments reported in this paper were housed and handled according to animal experimental protocols approved by the CIEMAT Animal Ethical Committee, in strict adherence to the guidelines stated in the International Guiding Principles for Biomedical Research Involving Animals established by the Council for International Organisations of Medical Sciences (CIOMS). All experimental animal procedures were approved by the Competent Authority of the Regional Government of Madrid, Spain (PROEX 094/15 and 294.8/2020).

A triple-negative breast cancer orthotopic xenograft model was generated by injecting 3×10^6 MDA 231-BrM2–831 cells in 100 μL of a 1:1 mix of PBS with Matrigel (Corning, Corning, NY) into the lower left 5th mammary fat pad of 13/14-week-old female athymic Nude-Foxn1nu immunodeficient mice (ENVIGO RMS SPAIN, Barcelona, Spain). Cells were allowed to engraft and tumours were measured once per week using a calliper.

Mice were sacrificed when the tumour mass reached a maximum size of 1 cm^3, tumour ulceration was observed, or mice were symptomatic from their tumours, which included signs of lethargy, poor grooming, weight loss, and hunching.

2.5. ^{89}Zr-LEM2/15 biodistribution

Mice were randomized into three groups and PET/CT imaging studies were performed 1, 2, 4, and 7 days after administration of [^{89}Zr]Zr-Df-LEM2/15 ($n = 7$ and $n = 3$ for non-blocked and blocked groups, respectively) via the caudal tail vein in tumour-bearing mice; the blocked group was intravenously administered with 280 μg of unlabelled LEM2/15 45 min prior to the [^{89}Zr]Zr-Df-LEM2/15 injection. A separate control group of tumour-bearing mice ($n = 4$) was injected with the [^{89}Zr]Zr-Df-IgG1k isotype control antibody as a second negative control.

Static PET imaging acquisition (2 beds whole body PET acquisition, 20 min/bed, energy window 250–700 keV) was performed using a small-animal Super Argus 2r PET/CT scanner (Sedecal, Madrid, Spain) under anaesthesia (isoflurane, 3 % induction, and 2 % maintenance in 100 % O$_2$). CT images were acquired immediately after PET acquisition for precise localisation of radiotracer accumulation using the following parameters: 150 μA, 45 kV, 360 projections, 8 shots, and standard resolution. PET image reconstruction was accomplished using a 2D-OSEM (Ordered Subset Expectation Maximisation (OSEM) algorithm (16 subsets and two iterations) with random and scatter correction. Images

were analysed using Biomedical Image Quantification Software PMOD (version 4.302). Manually drawn regions of interest (ROIs) in tumours and healthy tissues were used to determine radiotracer accumulation in organs (expressed as the percentage of injected dose per gram tissue, % ID/g) which were selected from PET images using CT anatomical guidelines.

For ex vivo biodistribution analysis, following the imaging procedure mice were euthanised on day 7 after radiotracer inoculation by cervical dislocation under anaesthesia with isoflurane in O_2, and blood was immediately collected into counting tubes by cardiac puncture. Organ tissues (heart, lungs, liver, spleen, kidneys, muscle, bone, fat, stomach, gut, and brain) and tumours were excised, wet-weighed, and counted for radioactivity using a 2470 Wizard^2 gamma counter (PerkinElmer, Waltham, MA, USA). A standard sample of the injected dose values for ^{89}Zr 511 keV photons was then determined in counts per minute (cpm) by measuring samples. The data were background- and decay-corrected, and tissue activity was expressed as the percentage injected dose per gram of tissue (%ID/g).

2.6. Pharmacokinetics

For pharmacokinetic studies, blood samples were collected on day 7 post-dosing in heparinised tubes and centrifuged at 3000 rpm for 10 min to separate the plasma. The blood/plasma ratio obtained was used to determine the plasma concentrations (%ID/mL) at each time point from the blood activity measured by drawing an ROI on the outflow area of the heart in the PET/CT studies. Calculated plasma concentrations were plotted against the time post-injection. The pharmacokinetic parameters were estimated by non-compartmental analysis (NCA) using the add-in program PKSolver. The terminal slope was automatically estimated using a regression with the largest adjusted R^2 value. The area under the curve (AUC) was calculated using the log-linear trapezoidal method, and other parameters, including the terminal half-life ($t_{1/2}$), mean residence time (MRT), clearance (Cl), and steady-state volume of distribution (V_{ss}) were also calculated.

2.7. Patlak linearisation for target engagement

The different contributions of ^{89}Zr-mAbs uptake to the PET signal was evaluated using Patlak linearisation. The signal observed on PET tumour imaging can be separated in two components: (1) *reversible,* radiolabelled mAb in the plasma and interstitial space of the tumour that, after some time, is in steady-state equilibrium with the plasma plus radiolabelled mAb reversibly bound to the target receptor or non-target binding sites; (2) *irreversible,* which reflects irreversible binding followed by internalisation after binding to target receptors plus non-specific internalising binding, such as pinocytosis and subsequent lysosomal proteolytic degradation.

^{89}Zr-mAb is administered to the blood plasma, distributed, and reversibly present inside the blood fraction and interstitial space of the tumour. Subsequently, several non-specific and specific binding processes occur, which both could be reversible and irreversible; the binding of mAb to the Fcγ receptor (FcγR) on immune effector cells and to the neonatal Fc receptor (FcRn) within vascular endothelial cells and
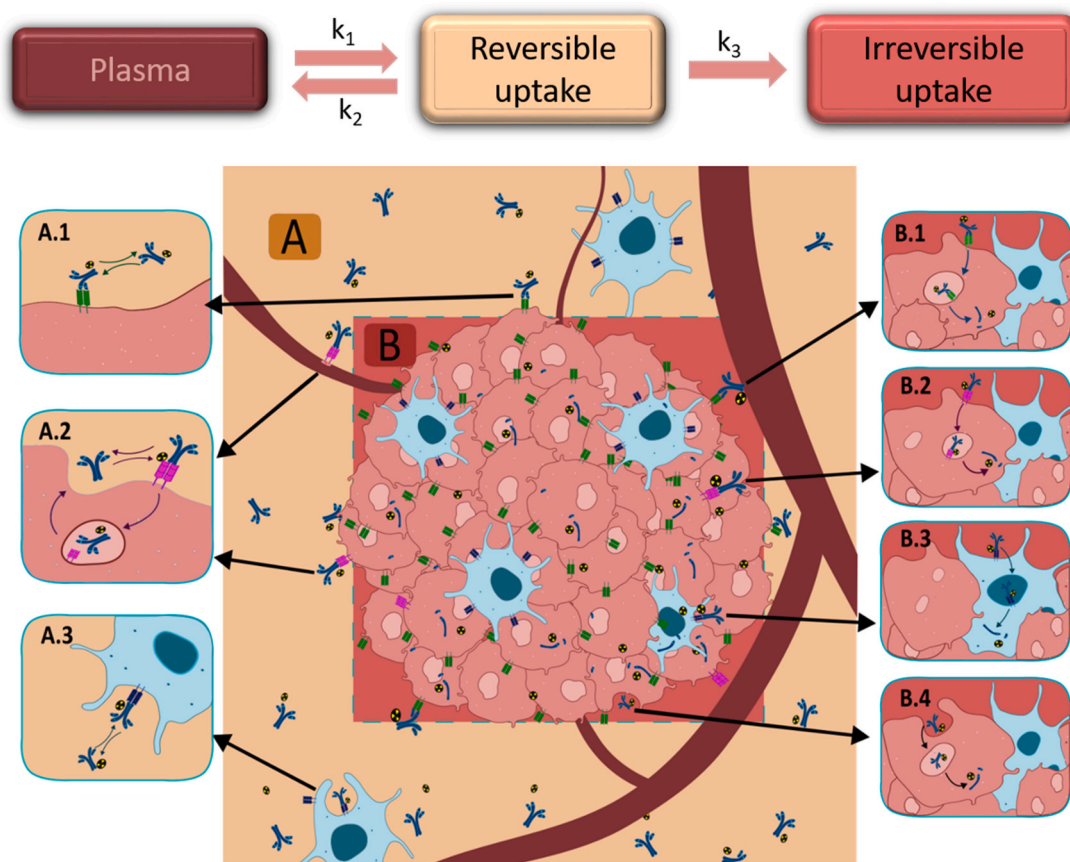

Fig. 1. A two-tissue compartmental model with irreversible uptake. (A) The reversible component includes: binding of LEM2/15 to its target MT1-MMP (A.1), neonatal Fc receptor-based recycling of mAb in tumour and vascular endothelial cells (A.2), and binding of mAb to the Fcγ receptor on immune effector cells outside the tumour (A.3). (B) The irreversible component consists of specific uptake due to target binding and internalisation of ^{89}Zr-LEM2/15-MT1-MMP complex (B.1) and nonspecific uptake due to residualisation of ^{89}Zr-mAb inside the cells after its internalisation by lysosomal degradation of mAbs not salvaged by FcRn/FcγR recycling (B.2/B.3) and fluid phase pinocytosis (B.4). The illustration of reversible and irreversible components of tumour radioactivity for Patlak modelling was created with Inkscape (https://inkscape.org).

cancer cells are non-specific processes, whereas the binding to its target is considered specific. The irreversible component includes specific uptake due to target engagement (target binding and internalisation of [89]Zr-mAb-target complex) and non-specific uptake due to [89]Zr-mAb internalisation within cells by fluid phase pinocytosis and lysosomal degradation of mAbs, not salvaged by FcRn/FcγR recycling; this is followed by residualisation of [89]Zr inside the cell, leading to the accumulation of PET signal within the region of interest (Fig. 1).

The equations for radiolabelled mAb concentration in the tumour, ROI(t), for the two-compartment model (Fig. 1) with first-order mass transfer are as follows:

$$\frac{dC_r(t)}{dt} = K_1 \bullet C_p(t) - k_2 \bullet C_r(t) - k_3 \bullet C_r(t) \tag{1}$$

$$\frac{dC_{ir}(t)}{dt} = k_3 \bullet C_r(t) \tag{2}$$

$$ROI(t) = C_r(t) + C_{ir}(t) + V_B \bullet C_B(t) \tag{3}$$

where K_1, k_2, and k_3 are the first-order rate constants, $C_p(t)$ is the concentration of radiolabelled mAb in arterial plasma estimated either from a heart image ROI or from blood sampling, $C_B(t)$ is the total radioactivity concentration in the tumour vasculature, and V_B is the volume fraction of blood in the tissue. $C_r(t)$ and $C_{ir}(t)$ are the concentrations of intact and degraded mAbs in the tumour, respectively. The [89]Zr, as a residualized radionuclide, remains in cells after antibody internalisation.

Rearranging Eq. (1) gives an equation for $C_r(t)$, which is substituted into Eq. (2) to solve $dC_{ir}(t)/dt$:

$$C_r(t) = \frac{K_1}{k_2 + k_3} \bullet C_p(t) - \left(\frac{1}{k_2 + k_3}\right) \bullet \frac{dC_r(t)}{dt} \tag{4}$$

$$\frac{dC_{ir}(t)}{dt} = \frac{K_1 \bullet k_3}{k_2 + k_3} \bullet C_p(t) - \left(\frac{k_3}{k_2 + k_3}\right) \bullet \frac{dC_r(t)}{dt} \tag{5}$$

The integration of Eq. (5) gives the solution for $C_{ir}(t)$:

$$C_{ir}(t) = \frac{K_1 \bullet k_3}{k_2 + k_3} \bullet \int_0^t C_p(t)dt - \left(\frac{k_3}{k_2 + k_3}\right) \bullet C_r(t) \tag{6}$$

If Eq. (6) is substituted into the expression for ROI(t) in Eq. (3), the following equation is obtained:

$$ROI(t) = \frac{K_1 \bullet k_3}{k_2 + k_3} \bullet \int_0^t C_p(t)dt + \frac{k_2}{k_2 + k_3} \bullet C_r(t) + V_B \bullet C_B(t) \tag{7}$$

The following Equation is obtained dividing the Eq. (7) by $C_p(t)$:

$$\frac{ROI(t)}{C_p(t)} = \frac{K_1 \bullet k_3}{k_2 + k_3} \bullet \frac{\int_0^t C_p(t)dt}{C_p(t)} + \frac{k_2}{k_2 + k_3} \bullet \frac{C_r(t)}{C_p(t)} + \frac{V_B \bullet C_B(t)}{C_p(t)} \tag{8}$$

The ROI(t)/$C_p(t)$ was then plotted on the y-axis and the integral of $C_p(t)$ (i.e., AUC) over $C_p(t)$ on the x-axis (Patlak plot). The condition for the linearity of the plot based on Eq. (8) is that the intercept $(k_2/(k_2 + k_3))\cdot(C_r(t)/C_p(t)) + V_BC_B(t)/C_p(t)$ is constant (distribution volume, V_T). After some time t > t', the reversible compartment concentration follows the plasma concentration such that $C_r(t)/C_p(t)$ and $C_B(t)/C_p(t)$ are constant, which ensures that the intercept is constant [26]. The slope of the linear phase of the plot represents the net influx rate of irreversible uptake of the radiotracer $(K_i = (K_1\cdot k_3)/(k_2 + k_3))$.

Wang et al. described a modified Patlak model which replaced the plasma concentration by the heart uptake from noninvasive PET imaging [27]. With these assumptions, tumour uptake (%ID/g) can be defined as a function of the in vivo heart uptake (%ID/g) with PET imaging using the following equation:

$$\frac{Tumour\,uptake(t)}{Heart\,uptake(t)} = B \times \frac{AUC_0^t}{Heart\,uptake\,(t)} + A \tag{9}$$

where A is the intercept, associated with blood volume in the tumour and the normalised tracer concentration from the reversible compartment (V_T, expressed in mL·cm^{-3}); B is the slope, related to the irreversible compartment (Ki, expressed in mL·g^{-1}·d^{-1}); and AUC_0^t is the integral of heart uptake (%ID/g) over time. The initial heart uptake (% ID/g) was estimated from the heart uptake (%ID/g)-time curve (0-t) by non-compartmental analysis.

Another important consideration for the design of [89]Zr-immuno-PET studies is that scans obtained with at least three late time points, when a steady-state equilibrium is reached, are required for Patlak linearisation to assess whether the data can be fitted to a straight line and, therefore, to determine reversible and irreversible uptake [28]. An r-value >0.9 was considered acceptable. Linear fits with an r-value <0.9 were excluded from the analysis.

The reversible and irreversible contributions to the tumour uptake of [89]Zr-mAb (expressed as %ID/g) at each time point were calculated as:

$$Tumour\,uptake_t^{rev} = V_T*Heart\,uptake_t \tag{10}$$

$$Tumour\,uptake_t^{irr} = K_i*AUC_0^t \tag{11}$$

In addition, the percentage of the reversible and irreversible components (Tumour-associated activity) was calculated as $Tumour\,uptake_t^{rev\,or\,irr} *100/(Tumour\,uptake_t^{rev} + Tumour\,uptake_t^{irr})$ (%).

2.8. Pharmacodynamic study

2.8.1. Animal model

A triple-negative subcutaneous breast cancer xenograft model was generated for subsequent pharmacodynamics studies (imaging and ex vivo studies) by injecting 5×10^5 MDA 231-BrM2-831 cells in 100 μL of a 1:1 mix of PBS with Matrigel (Corning, Corning, NY) into the lower left right flank of 5 weeks female athymic Nude-Foxn1nu immunodeficient mice (ENVIGO RMS SPAIN, Barcelona, Spain).

2.8.2. In vivo targeted radionuclide therapy with [^{177}Lu]Lu-DOTA-LEM2/15

Upon the detection of palpable tumour, mice were randomized into one of three therapy cohorts and intravenously injected with 0.9 % sterile saline ($n = 13$) or [^{177}Lu]Lu-DOTA-LEM2/15. The radio-immunoconjugate was administered either as a single dose ($n = 10$) or through a 3-dose regimen ($n = 9$); the first dose was administered 13 days after tumour cells implantation and this was repeated 15 days and 30 days later. Tumour volume was measured by CT just before starting treatment; CT was performed in a small-animal Super Argus 3r PET/CT scanner (Sedecal, Spain) with the following acquisition parameters: 500 μA, 30 kV, 360 projections, 1 shot and 4 × 4 binning. The average tumour volume was 36 ± 16 mm^3 (n = 13), 29 ± 18 mm^3 ($n = 7$) and 37 ± 16 mm^3 (n = 9) for control, single dose and 3-dose regimen groups respectively. Following therapy initiation, tumour volumes and weights were measured 1–2 times per week for 12 weeks or until mice reached a defined end point. Tumour dimensions, including length and width, were measured using a digital calliper, and tumour volume was calculated assuming a ellipsoidal shape: $4\pi/3 \times (width/2)^2 \times (length/2)$. Three mice were euthanised 7 days after administration of the first dose, the blood was sampled via cardiac puncture and tumours were collected and weighed for ex vivo analysis of radioactivity using a 2470 Wizard2 solid scintillation counter (PerkinElmer, Waltham, MA, USA).

Endpoint criteria were defined as tumour volume exceeding 1 cm^3 (primary endpoint) or if they were observed to experience severe poor health, tumour ulceration, lethargy, poor grooming, weight loss or hunching.

2.8.3. Tumour growth rate

To obtain the tumour growth rates, exponential growth rate was assumed and tumour volume (TV) was defined as follows:

$$TV = TV_0 \bullet e^{k \bullet t}$$

where TV_0 denotes the initial tumour volume, k is the exponential growth rate, and t is the time. Tumour doubling time (DT) is defined by the number of days required for a tumour to double its volume and is calculated as $DT = Ln(2)/k$. For each group, TV was fitted to the above Equation by using the OriginPro 8 software; the data were weighted by the Statistical weighting method $(1/y)$. The correlation coefficient R^2 was computed for each exponential fit.

2.9. Immunohistochemistry

Tumours were fixed in 10 % neutral buffered formalin (Sigma-Aldrich, Saint Louis, MO), paraffin-embedded, and cut at 3 μm, mounted in Superfrost® Plus slides and dried overnight. For the analysis of MT1-MMP expression, immunohistochemical staining was performed using anti-MT1-MMP LEM 2/15 antibody at a 1:400 dilution from culture supernatant after antigen retrieval with low pH buffer on the Autostainer platform (Dako, Santa Barbara, CA, USA). The sections were then counterstained with haematoxylin. Whole slides were captured using an AxioScan Z1 slide scanner (Zeiss, Oberkochen, Germany). For the analysis, an appropriate script was developed using Zen Blue Software (Version 3.1, additional module for analysis).

For immunohistochemistry (IHC) of phosphorylated histone H2AX (γH2AX), which has been demonstrated as a DNA damage marker both in vitro and in vivo, an automated immunostaining platform Ventana Discovery ULTRA (Roche, Madrid, Spain) was used. Antigen retrieval was performed with CC1 buffer (Roche, Madrid, Spain); endogenous peroxidase was blocked (hydrogen peroxide at 3 %) and slides were then incubated with the appropriate mouse monoclonal anti-γH2AX primary antibody (clone JBW301; 1/25000, Merck KGaA, Darmstadt, Germany). After the primary antibody, slides were then incubated with the corresponding secondary antibodies (rabbit anti-mouse, Abcam, Cambridge, UK) and visualisation systems (Omni Map anti-rabbit, Ventana, Roche, Madrid, Spain; Bond Polymer Refine Detection, Bond, Leica, Wetzlar, Germany) conjugated with horseradish peroxidase. The immunohistochemical reaction was performed using 3,30-diaminobenzidine tetrahydrochloride (DAB) as a chromogen (ChromoMap DAB, Ventana, Roche, Madrid, Spain) and nuclei were counterstained with Carazzi's haematoxylin. Finally, slides were dehydrated, rinsed and mounted with permanent mounting medium for microscopic evaluation. Positive control sections known to be primary antibody positive were included for each staining run. Whole slides were captured and digitalized using an AxioScan Z1 slide scanner (Zeiss, Oberkochen, Germany). For the analysis, an appropriate script was developed using QuPath v0.5.0 [29] and total versus positive cells were automatically quantified. The total number of cells was determined using the haematoxylin staining whereas the DAB staining was used to quantify the percentage of positive cells.

2.10. Statistical analyses

Two-way mixed ANOVA test was used to evaluate the pharmacokinetics and biodistribution of the ^{89}Zr-labelled mAbs in the subcutaneous xenograft. A one-way ANOVA was conducted to determine if the tumour growth rate (DT value) and percentage of γ-H2AX positive cells was different for groups. The threshold for statistical significance was set at $P < 0.05$. All statistical analyses were performed using SPSS 14.0.

3. Results

3.1. Characterisation of radiolabelled-mAbs

The Df-mAb conjugates were prepared using a 5-fold molar excess of p-SCN-Bn-Deferoxamine. The radiolabelling with ^{89}Zr proceeded at room temperature, and the radiochemical yields were in the range of 65 % to 75 %. Molar activities (specific activity) of 2.74 ± 0.67 and $2.51 \pm$

0.09 GBq/μmol were achieved for [^{89}Zr]Zr-Df-LEM2/15 and [^{89}Zr]Zr-Df-IgG, respectively, with >95 % radiochemical purity as confirmed by HPLC-SEC (Supplementary Fig. S1).

LEM2/15 forms a high-affinity complex with MT1-MMP ($K_D = 0.39 \pm 0.05$ nM) as reported previously by Udi et al. [30]. The affinity of Df-LEM2/15 and [^{89}Zr]Zr-Df-LEM2/5 was tested against the catalytic domain of recombinant MT1-MMP (CAT-MT1-MMP) and compared with the binding of the intact antibody. Fig. 2A shows the ELISA binding curves, indicating that the conjugation and radiolabelling had no effect on the binding; thus, the intact antibody, Df-LEM2/15 and [^{89}Zr]Zr-Df-LEM2/5 possess comparable binding affinities at the nanomolar range with $K_D = 0.264$, 0.312, and 0.412 nM, respectively.

The biologically active fraction or immunoreactive fraction (IRF) of the [^{89}Zr]Zr-Df-LEM2/5 was determined by the Lindmo antigen excess method. The total amount of radioactivity added to the wells divided by the specifically bound to the antigen coated wells (T/B) was plotted vs l/antigen concentration (Fig. 2B). There was a very good linear relationship between T/B vs l/antigen concentration ($R^2 = 0.9698$). When the best-fit line was extrapolated to the ordinate, the intercept yielded the inverse of the IRF at infinite antigen excess (l/Y). The intercept was 0.9437 and consequently the IRF was about 100 %; this result shows that the immunoreactivity is preserved and is therefore considered optimal for in vivo studies.

DOTA-LEM2/15 was also successfully labelled with ^{177}Lu. The radiochemical yield and radiochemical purity of [^{177}Lu]Lu-DOTA-LEM2/15 were about 35–40 % and $\geq$ 95 %, respectively. The radiochemical yields were slightly lower than for radiosynthesis with ^{89}Zr. As in the case of ^{89}Zr-labelled LEM2/15, the DOTA conjugation and ^{177}Lu-radiolabelling had no effect on the binding of the antibody to CAT-MT1-MMP and with comparable binding affinities at the nanomolar range ($K_D = 0.140$, 0.154, and 0.083 nM for intact antibody, DOTA-LEM2/15 and [^{177}Lu]Lu-DOTA-LEM2/5, respectively) (Fig. 2A). Therefore, it is considered that [^{177}Lu]Lu-DOTA-LEM2/5 is suitable for the in vivo therapy study.

3.2. Pharmacokinetics and biodistribution of [^{89}Zr]Zr-Df-mAb using PET/CT imaging

PET/CT imaging studies in female mice bearing MDA 231-BrM2–831 cells orthotopic tumour xenografts were performed 1, 2, 4 and 7 days after administration of [^{89}Zr]Zr-Df-IgG (0.67 ± 0.03 MBq; 48 ± 1 μg; $n = 4$) or [^{89}Zr]Zr-Df-LEM2/15 (0.83 ± 0.17 MBq; 59 ± 10 μg; $n = 7$ and 0.83 ± 0.03 MBq; 55 ± 2 μg; $n = 3$ for non-blocked and blocked groups, respectively) via the tail vein in tumour-bearing mice.

3.2.1. Pharmacokinetics

The plasma levels gradually decreased with time for each group (Fig. 3), although the [^{89}Zr]Zr-Df-IgG levels were significantly higher than both plasma [^{89}Zr]Zr-Df-LEM2/15 (non-blocked and blocked) concentrations from 2 days post-administration. NCA was used to compare the kinetics of the radiolabelled-mAbs in plasma. The pharmacokinetic parameters are summarized in Table 1. There was no statistically significant difference between non-blocked and blocked LEM2/15 in the estimated PK parameters. However, the biological terminal half-life and MRT were significantly higher after [^{89}Zr]Zr-Df-IgG injection than after non-blocked/blocked [^{89}Zr]Zr-Df-LEM2/15 ($p < 0.0005$). The AUC also increased for the [^{89}Zr]Zr-Df-IgG due to its slower total blood clearance (0.52 ± 0.02 mL/d vs 1.1 ± 0.2 and 1.0 ± 0.2 mL/d for non-blocked and blocked [^{89}Zr]Zr-Df-LEM2/15, respectively; $p = 0.004$ and $p = 0.021$).

3.2.2. Biodistribution

To examine the in vivo biodistribution of the radiolabelled-mAbs, the uptake in tumours and healthy tissues was determined by PET imaging (Table S1). Fig. 4A illustrates the representative maximum intensity projection (MIP) images from the PET imaging in the tumour-bearing
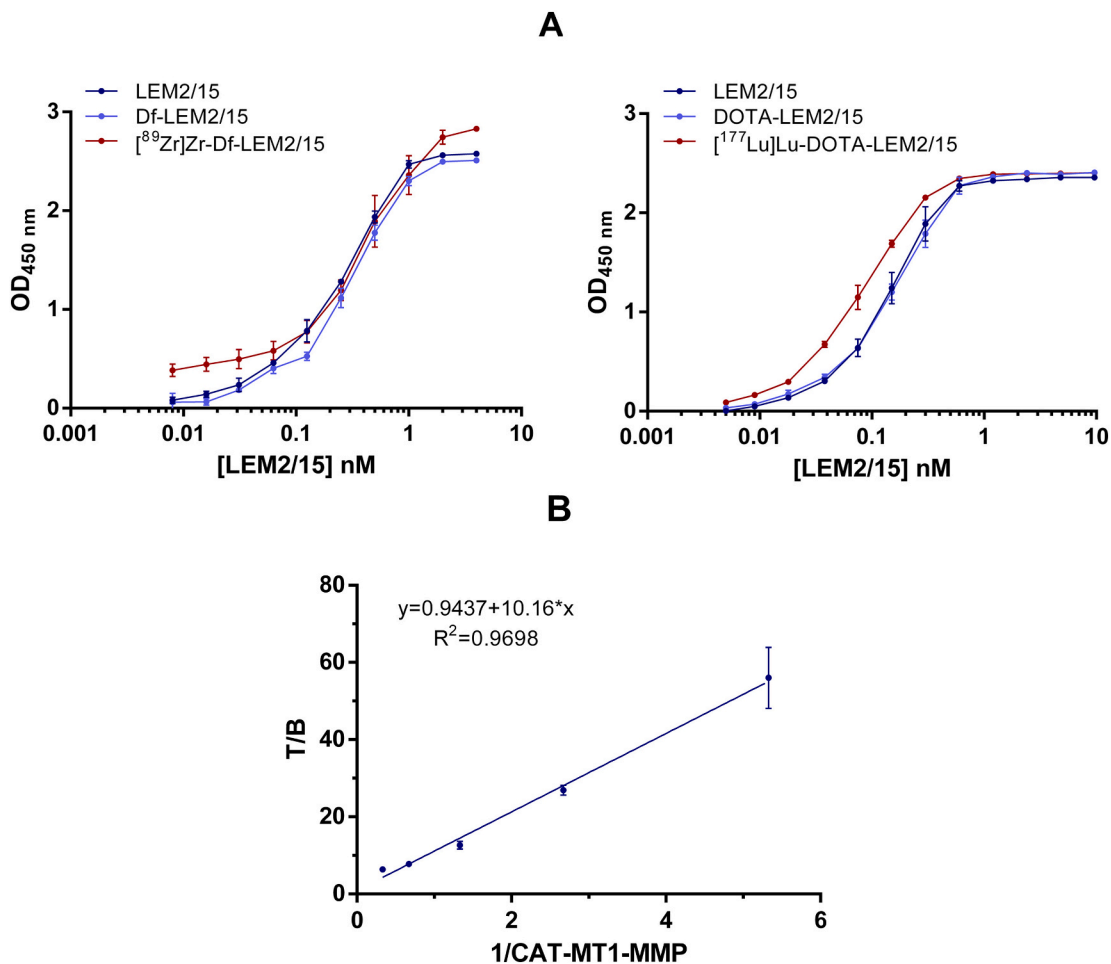
A

B

$$y = 0.9437 + 10.16 * x$$
$$R^2 = 0.9698$$

Fig. 2. (A) Binding curves for intact LEM2/15, Df/DOTA- LEM2/15 and [^{89}Zr]Zr-Df-LEM2/15 or [^{177}Lu]Lu-DOTA-LEM2/15 to CAT-MT1-MMP, indicating that deferoxamine/DOTA conjugation to LEM2/15, and ^{89}Zr/^{177}Lu-radiolabelling had no effect on the binding of LEM2/15 to CAT-MT1-MMP (B) Plot of T/B vs l/[CAT-MT1-MMP] for [^{89}Zr]Zr-Df-LEM2/15; the immunoreactive fraction of [^{89}Zr]Zr-Df-LEM2/5, determined by the inverse of the intercept on the ordinate, was about 100 %. Error bars represent SD of an ELISA or IRF assay done with samples in triplicate.
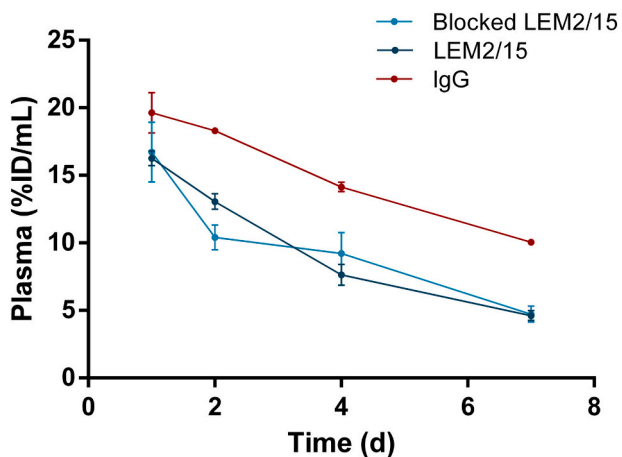
Fig. 3. Time activity curve of [^{89}Zr]Zr-Df-IgG and non-blocked/blocked [^{89}Zr]Zr-Df-LEM2/15 plasma levels in TNBC grafted mice.

mice injected with 1 ± 0.2 MBq of [^{89}Zr]Zr-Df-mAb. MDA 231-BrM2-831 tumour xenografts were visible throughout the study period (1–7 days) in the non-blocking LEM2/15 group, whereas tumours were less visualized in the blocking LEM2/15 group, demonstrating MT1-MMP specificity. Tumours were visible with lower intensity in IgG1 isotype

Table 1
Mean pharmacokinetic parameters estimated by non-compartmental analysis after i.v. injection of [^{89}Zr]Zr-Df-mAbs. Data are expressed as mean $\pm$ SD.

PK Parameters	[^{89}Zr]Zr-Df-mAb		
	IgG	LEM2/15 non-blocked	LEM2/15 blocked
$t_{1/2}$ (d)	5.8 ± 0.3	3.3 ± 0.6	3.4 ± 0.2
AUC (%ID·d/mL)	192 ± 6	94 ± 16	99 ± 23
MRT (d)	8.5 ± 0.5	4.8 ± 0.7	4.8 ± 0.2
Cl (mL/d)	0.52 ± 0.02	1.1 ± 0.2	1.0 ± 0.2
V_{ss} (mL)	4.4 ± 0.3	5.2 ± 0.5	5.1 ± 1.2

$t_{1/2}$: Terminal half-life time, AUC: Area Under Curve, MRT: Mean residence time, Cl: Clearance, V_{ss}: Steady-state volume of distribution.

control antibody group, likely due to the non-specific uptake. From these biodistribution studies, tumour tissues were prepared for MT1-MMP IHC staining to confirm that the [^{89}Zr]Zr-Df-LEM2/15 mAb uptake in the tumour represented specific targeting to MT1-MMP (Fig. 4B).

A two-way mixed analysis of variance was run to determine if the tumour-to-blood ratio changed differently over time depending of the injected radiotracer. A statistically significant interaction between the mAb-based radiotracer and time on the tumour-to-blood ratio ($p < 0.0005$) was found (Fig. 5). Tumour-to-blood ratio of [^{89}Zr]Zr-Df-LEM2/15 increased over time and was significantly higher than the isotype control group and the blocked LEM2/15 group from 4 days post-
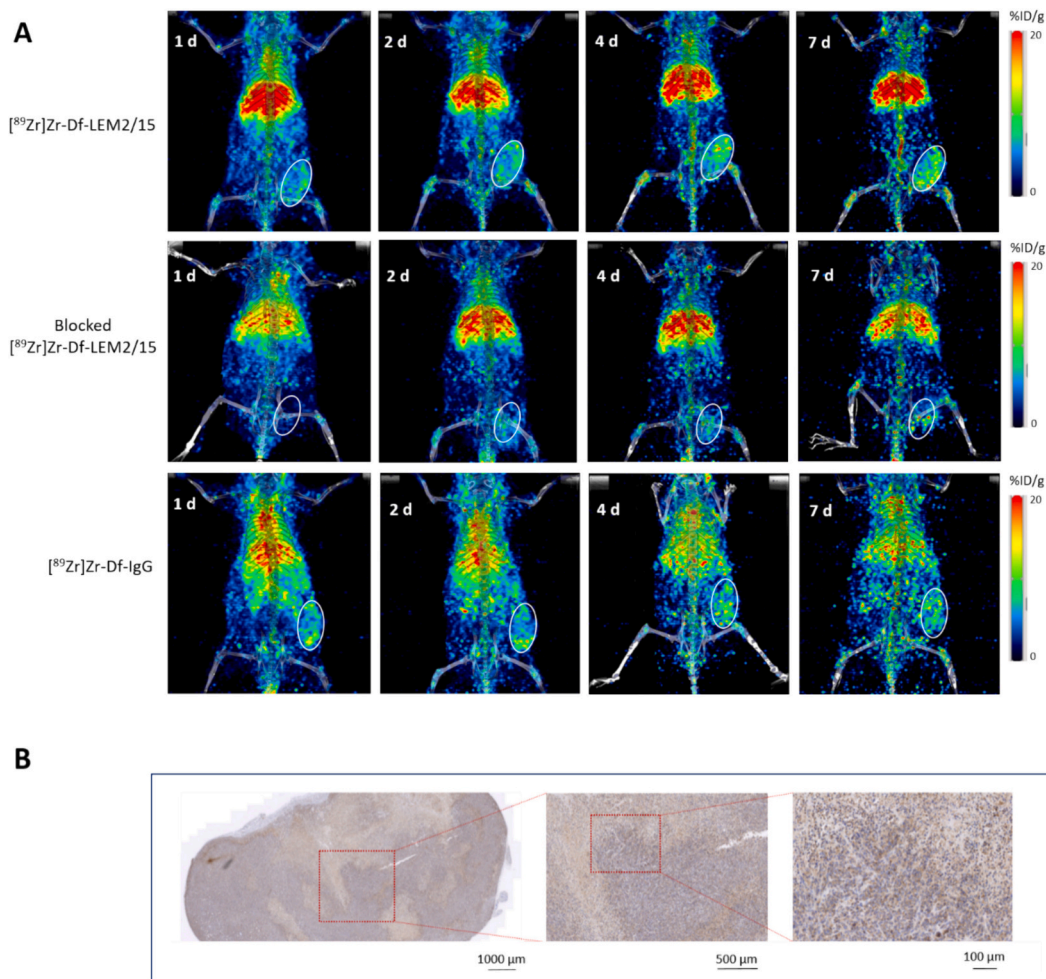
Fig. 4. (A) MIP PET/CT images in subcutaneous MDA 231-BrM2-831 tumour-bearing mice at different time points after i.v. injection of different tracers: [^{89}Zr]Zr-Df-LEM2/15 (blocked and non-blocked) and [^{89}Zr]Zr-Df-IgG, white circles indicates the tumour location; (B) images (x20 magnification) of MT1-MMP IHC-stained tumour sections.
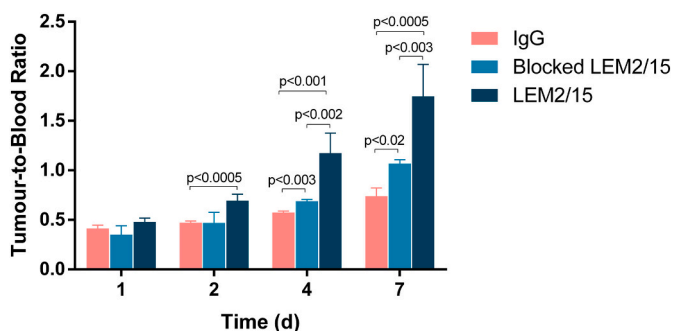

Fig. 5. Tumour-to-blood ratios based on %ID/g at 1, 2, 4 and 7 days post-injection of non-blocking/blocking [^{89}Zr]Zr-Df-LEM2/15 and [^{89}Zr]Zr-Df-IgG. *p*-values are indicated in the figures above the two groups compared.

injection. Notably, the tumour-to-blood ratios reached their highest values of 0.74 ± 0.08, 1.07 ± 0.04 and 1.75 ± 0.32 at 7 days post-injection for [^{89}Zr]Zr-Df-IgG, blocked [^{89}Zr]Zr-Df-LEM2/15 and non-blocked [^{89}Zr]Zr-Df-LEM2/15 groups, respectively, due to the specific retention of the [^{89}Zr]Zr-Df-LEM2/15-derived radioactivity after internalisation and catabolism of the antibody as well as its faster blood clearance compared with [^{89}Zr]Zr-Df-IgG (Table 1).

PET imaging revealed radiotracer uptake in healthy tissues of MDA 231-BrM2-831 tumour-bearing mice (Fig. 4A). Consistent with these results, ex vivo biodistribution at day 7 post-injection showed highest ^{89}Zr-tracers uptake in liver (5.1 ± 1.1, 11.1 ± 1.9 and 12.3 ± 2.5 %ID/g for IgG-, blocked/non-blocked LEM2/15-based radiotracers, respectively), tumour (5.3 ± 1.2, 3.5 ± 0.4 and 6.8 ± 1.3 %ID/g for IgG, blocked/and non-blocked LEM2/15-based radiotracers, respectively), spleen (4.0 ± 0.4, 3.7 ± 0.7 and 4.4 ± 1.3 %ID/g for IgG, blocked/non-blocked LEM2/15-based radiotracers, respectively) and bone (3.9 ± 1.1, 4.1 ± 0.3 and 4.3 ± 1.7 %ID/g for IgG-, blocked/non-blocked LEM2/15-based radiotracers, respectively) (Fig. 6). Bone uptake likely indicates loss of ^{89}Zr from the Df chelate which was expected.

3.3. Target engagement of [^{89}Zr]Zr-Df-mAbs in vivo

Patlak plots were obtained for each radiotracer in the MDA 231-BrM2-831 tumours using all time points of the dynamic PET studies since equilibrium state was assumed for these time points ($t \geq 1$ day). An *r* value of >0.9 was obtained for 6 of 7 linear fits for [^{89}Zr]Zr-Df-LEM2/15, for 3 of 4 linear fits for [^{89}Zr]Zr-Df-IgG and for all linear fits for blocked [^{89}Zr]Zr-Df-LEM2/15, therefore we assumed that data were consistent with the assumptions under the Patlak method. The fitting equation shows that the intercept (A) of each group was basically the same, while the slope (B) varied with the radiotracer (Table 2). Values for V_T (associated to the reversible uptake) were 0.395, 0.444, and 0.360 mL·cm^3 for [^{89}Zr]Zr-Df-IgG, non-blocked [^{89}Zr]Zr-Df-LEM2/15 and blocked [^{89}Zr]Zr-Df-LEM2/15, respectively. Nonspecific, irreversible uptake is reflected by value for K_i for IgG, 0.033 mL·g^{-1}·d^{-1}. In the
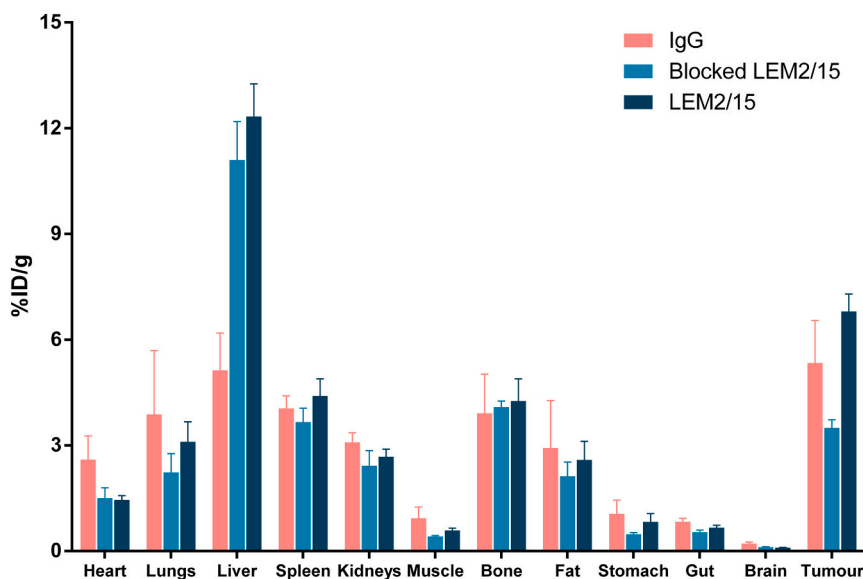
Fig. 6. Biodistribution ex vivo by PET imaging at 7 days post-injection of non-blocked/blocked [^{89}Zr]Zr-Df-LEM2/15 and [^{89}Zr]Zr-Df-IgG.

Table 2

Patlak linearisation showing distribution volume (V_T) and net influx rate (K_i) values, representing reversible and irreversible uptake, respectively. Data are expressed as mean with 95 % confidence interval (in parentheses). N = number of datasets with $r > 0.9$.

Treatment group	V_T (mL·cm^3)	K_i (mL·g^{-1}·d^{-1})	N
[^{89}Zr]Zr-Df-IgG	0.395 (0.364–0.425)	0.032 (0.015–0.050)	3
[^{89}Zr]Zr-Df-LEM2/15	0.444 (0.378–0.511)	0.085 (0.071–0.099)	6
Blocked [^{89}Zr]Zr-Df-LEM2/15	0.360 (0.180–0.539)	0.025 (0.020–0.030)	3

case of target engagement for [^{89}Zr]Zr-Df-LEM2/15, it is expected to observe an increased rate of irreversible uptake ($K_i = 0.085$ mL·g^{-1}·d^{-1}) as a consequence of MT1-MMP-binding followed by internalisation compared with the value for [^{89}Zr]Zr-Df-IgG. Thus, a 2.6-fold increase K_i (0.085 vs 0.033) for LEM2/15 was found compared with IgG for the tumour, indicating specific MT1-MMP engagement by irreversible uptake. Because of the competition for MT1-MMP binding, the tumour uptake must decrease with co-injection of unlabelled LEM2/15; a decreased K_i was observed for blocking (0.025 mL·g^{-1}·d^{-1}) compared with non-blocked [^{89}Zr]Zr-Df-LEM2/15 (0.025 vs 0.085) indicating a target saturation.

The reversible and irreversible contributions to the measured activity are shown in the Fig. 7. For [^{89}Zr]Zr-Df-LEM2/15, the irreversible contribution at 1 day post-injection, which corresponds mainly to the specific target engagement of the anti-MT1-MMP, was 18 ± 3 % of the tumour-associated activity. This contribution was only 8 ± 2 % after blocked [^{89}Zr]Zr-Df-LEM2/15 indicating saturable binding to MT1-MMP; the non-specific irreversible contribution for [^{89}Zr]Zr-Df-IgG was also 8 ± 1 %. The irreversible and reversible contribution over time allowed identification of the most relevant time point to study the irreversible binding part of LEM2/15, corresponding to the time point 7 days post-injection (Fig. 7). Thus, the irreversible binding of the [^{89}Zr]Zr-Df-LEM2/15 antibody to its target in tumour tissue contributed with 75 ± 5 % of the tumour-associated activity. These results demonstrate the specific uptake of LEM2/15 in MDA 231-BrM2–831 tumours mediated by MT1-MMP-binding, which could predict efficacy of LEM2/15-based treatments.

3.4. Pharmacodynamics study

The therapeutic efficacy of [^{177}Lu]Lu-DOTA-LEM2/15 was evaluated in female nude mice bearing MDA 231-BrM2-831 xenograft tumours. Mice bearing visible and palpable tumours were injected with 6.5 ± 0.5 MBq [^{177}Lu]Lu-DOTA-LEM2/15 (a single dose or three doses) or saline on day 13 post tumour cells inoculation. Ex vivo activity of [^{177}Lu]Lu-DOTA-LEM2/15 in tumour of three mice was measured via gamma-ray scintillation spectrometry 7 days after radioactive antibody post-injection. Similar uptake was found for [^{89}Zr]Zr-Df-LEM2/15 and [^{177}Lu]Lu-DOTA-LEM2/15 in tumours (6.80 ± 1.31 vs. 5.61 ± 0.66 % ID/g; $p = 0.183$), indicating tumour-targeting is not affected by radionuclide or chelator (p-SCN-Bn-Deferoxamine for ^{89}Zr versus DOTA-NHS for ^{177}Lu).

Monitoring of the mice did not reveal body weight loss over time in all groups (Fig. 8A). Tumour volume was monitored up to 12 weeks after treatment and the results are shown in Fig. 8B. Treatment with the ^{177}Lu-radiolabelled LEM2/15 3-dose regimen reduced tumour growth compared to the control group. The boxplot in Fig. 8C indicate that the variability in tumour doubling time was higher for the [^{177}Lu]Lu-DOTA-LEM2/15 3-dose regimen group than for both the single-dose regimen and control groups. Note, the tumour doubling time was longer in the [^{177}Lu]Lu-DOTA-LEM2/15 3-dose regimen treated group (50 days; 95 % confidence interval 33–67 d) compared to both the [^{177}Lu]Lu-DOTA-LEM2/15 single-dose regimen treated group (15 days; 95 % confidence interval 11–20 d; $p = 0.004$) and the control group (17 days; 95 % confidence interval 15–19 d; $p = 0.005$).

By immunostaining, we observed DNA double-strand break damage as measured by γH2AX-positive cells (Fig. 8D). The γH2AX IHC was performed in tumours at 63–70 days after starting therapy in control and single dose groups and 83 days for the 3-dose regimen group. Whereas the percentage of γH2AX-positive cells was similar between non-treated ($n = 4$) and [^{177}Lu]Lu-DOTA-LEM2/15 single-dose treated ($n = 5$) mice (4.2 ± 1.8 % and 4.8 ± 1.5 % respectively), this percentage was significantly higher for the [^{177}Lu]Lu-DOTA-LEM2/15 3-dose regimen treated group (12.2 ± 6.4 %; $n = 9$).

4. Discussion

A subset of MMPs is often over-expressed in breast cancer and is associated with the prognosis of the disease; they are therefore considered to be promising therapeutic targets for breast cancer [31]. Among
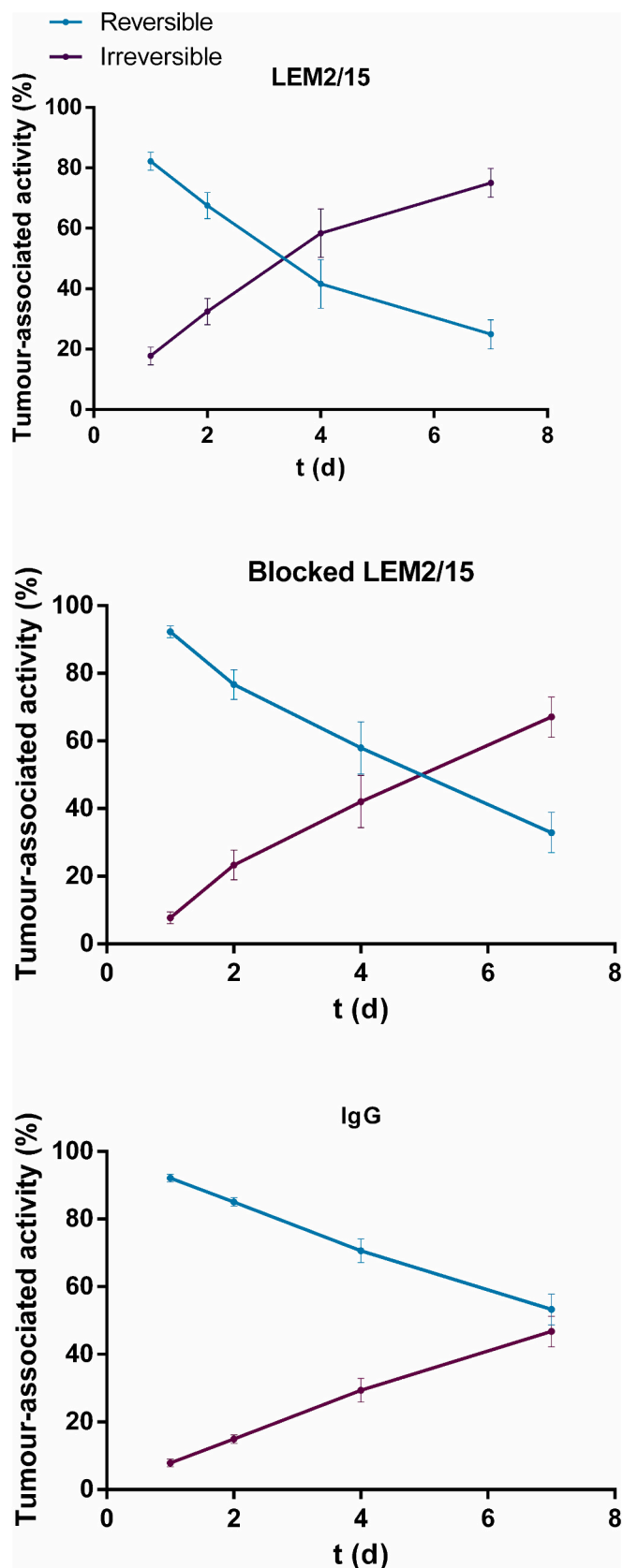
Fig. 7. Plots showing the estimation of reversible and irreversible radio-immunoconjugates fixation contributions to measured activity for tumour using Patlak linearisation. At the end of the study (7 days post-injection), 75 % of the tumour-associated activity corresponded to the irreversible uptake of [89Zr]Zr-Df-LEM2/15 and 45 % to [89Zr]Zr-Df-IgG.

these, several selective MT1-MMP inhibitory antibodies and antibody fragments have been described, including LEM2/15, an antibody generated using a cyclic peptide that mimics the MT1-MMP CAT domain V—B loop (residues 218–233) [32]. Our group has previously developed preclinical target-based approaches for PET imaging of MT1-MMP overexpression in glioblastoma and pancreatic ductal adenocarcinoma based on the full-length IgG murine anti-MT1-MMP monoclonal antibody LEM2/15, demonstrating that [89Zr]Zr-Df-LEM2/15 constitutes a promising radiotracer for noninvasive immuno-PET measurements of MT1-MMP expression in vivo [33,34].

In the present study, we developed an 89Zr-based immuno-PET technique that provides non-invasive imaging of the MT1-MMP expression in a triple-negative breast cancer model. Although the immunohistochemistry staining revealed a high tumour MT1-MMP expression, the tumour [89Zr]Zr-Df-LEM2/15 uptake was not very high. The immunohistochemistry staining offers a snapshot of MT1-MMP expression in a single slice, carefully chosen to be representative. On the other hand, the PET images present a 3D volume view, encompassing areas with varying levels of MT1-MMP uptake, including regions with low expression due to factors like necrosis; in the present work, we are detected by [18F]-FDG PET scan necrotic zones in the tumours of mice implanted with MDA-MB-231 cells (data not shown). This disparity can be explained by the heterogeneous distribution of MT1-MMP within the total volume of the tumour. Tumour heterogeneity, especially concerning MT1-MMP expression, is well-documented, and it's crucial to consider this aspect when interpreting results from different imaging modalities. The tumour-to-blood ratio of [89Zr]Zr-Df-LEM2/15 at 7 days post-injection was 2.4-fold higher than the isotype control IgG in TNBC tumour-bearing mice. When animals were pre-injected with excess unlabelled LEM2/15 mAb, tumour [89Zr]Zr-Df-LEM2/15 uptake was partially blocked on PET images and bio-distribution measurements. As shown in Fig. 3, blocking tumour uptake with unlabelled LEM2/15 mAb was not associated with reduced blood [89Zr]Zr-Df-LEM2/15 activity, indicating that binding to circulating MT1-MMP protein was minor. In addition, the tumour-to-blood ratio of [89Zr]Zr-Df-LEM2/15 at 7 days post-injection was 1.6-fold higher in the non-blocked group compared with the blocked-one. To maximise tumour uptake, unlabelled antibodies must be preloaded during immune-PET imaging [35]. However, the required blocking dose differs in a target- and antibody-dependent manner [36], and is greatly affected by the antibody treatment schedule at the time of tracer injection [37]. In our study, blockade was only performed with 4/5-fold excess LEM2/15; therefore, perhaps a larger excess migration has been used to significantly reduce the uptake in the tumour, for example, other studies have used up to 10/30-fold excess mAb [38].

Following the administration of radiolabelled LEM2/15, distribution throughout the body and uptake by tumour was observed (Fig. 4). Over time, tumour-to-blood ratios increased due to radiotracer binding to the tumour, residualisation of 89Zr in the tumour tissue, and clearance of the non-bound radiotracer from circulation and background organs/tissues. Tumour accumulation of [89Zr]Zr-Df-LEM2/15 is a consequence of the target location, target expression levels, target saturation, and internalisation of the radiolabelled mAb. In addition, several kinetic features, such as perfusion and vascularisation, may influence tumour visualisation [39]. The [89Zr]Zr-Df-LEM2/15 uptake was quantified using a PET scan, and the %ID/g was calculated. The measured uptake value includes both the contribution specific uptake due to MT1-MMP engagement and non-specific [89Zr]Zr-Df-LEM2/15 uptake, which includes part related to free radiotracer in blood or interstitial space volume fraction of the tissue that does not interact with the target, as well as 89Zr residualisation after LEM2/15 uptake and degradation by MT1-MMP-nonexpressing cells. A single uptake value is not able to predict efficacy in tumours and toxicity in normal tissues; therefore, 89Zr-immuno-PET studies should consider multiple-time-point acquisitions to assess non-specific uptake versus time because specific uptake increases over time, whereas early time points consist mainly of the blood volume
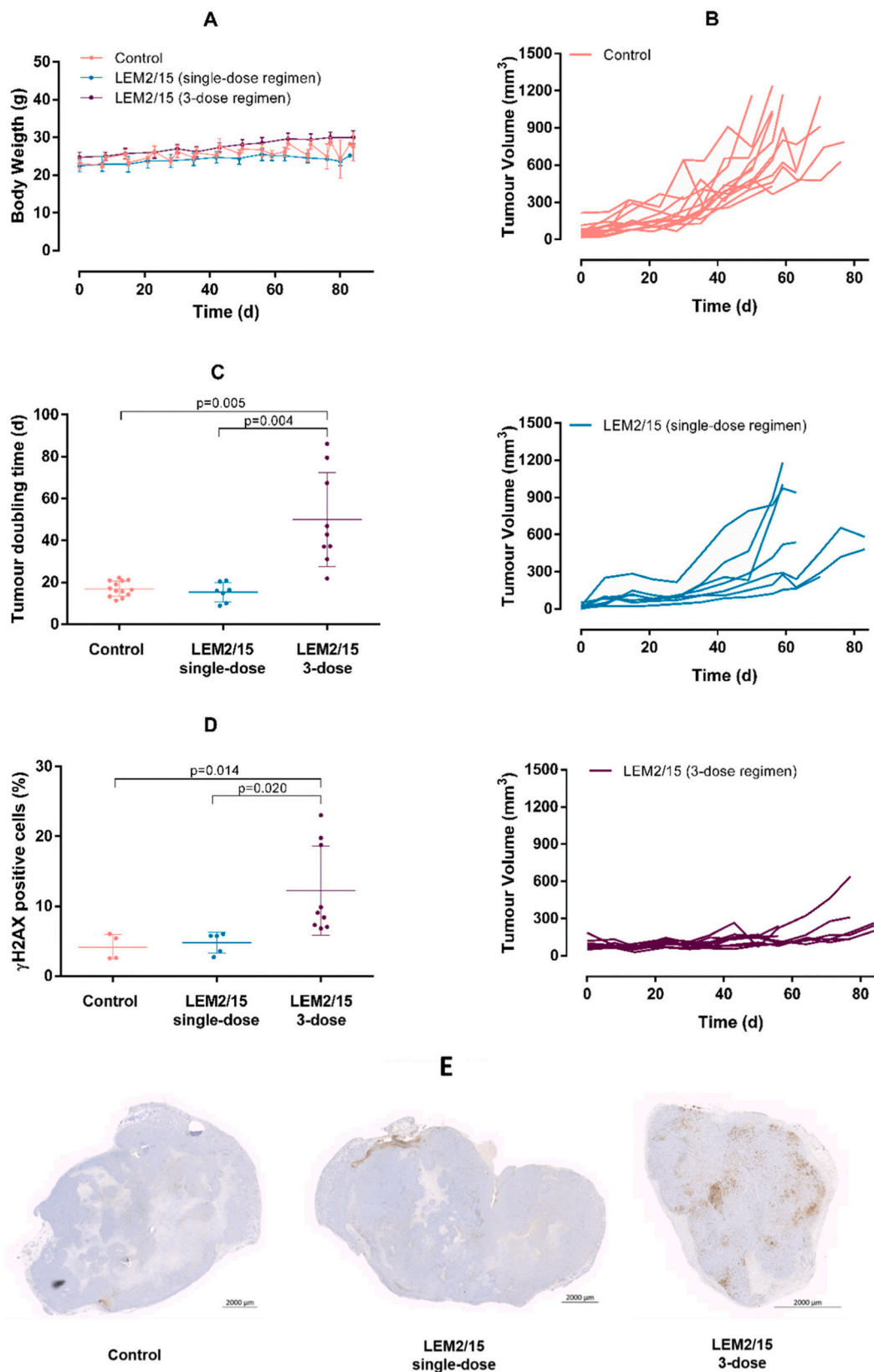
Fig. 8. (A) Body weight of mice of each group after treatment with vehicle (control group) or [^{177}Lu]Lu-DOTA-LEM2/15. (B) Tumour growth presented as change in tumour volume for each individual mouse over time. (C) Tumour doubling time (DT) was calculated based on the exponential curve fit of the tumour-volume measurements against time. With [^{177}Lu]Lu-DOTA-LEM2/15 3-dose regimen, tumour growth was significantly slower (longer DT, 50 days), compared to control and [^{177}Lu]Lu-DOTA-LEM2/15 single-dose regimen tumour growth (DT of 17 and 15 days respectively). (D) Percentage of γH2AX-positive cells in tumours of different treatment groups. This percentage was about 3-fold higher for the [^{177}Lu]Lu-DOTA-LEM2/15 3-dose regimen group. This high expression could be observed in the IHQ image corresponding to 3-dose regimen (E).

fraction. Patlak linearisation, using graphical evaluation of transfer constants of multiple-time ^{89}Zr-mAb tissue uptake data, can be used to estimate the reversible (quantified by the Patlak y-intercept, V_T) and irreversible (quantified by the Patlak uptake rate constant, K_i) contributions to the measured activity but cannot differentiate between specific and non-specific uptake because nonspecific uptake can be reversible or irreversible (^{89}Zr-residualisation in antigen non-expressing cells) [16,17]. Thus, the specific binding of LEM2/15 to its target (MT1-MMP) was determined using the Patlak linearisation method. The results indicated an irreversible uptake increase for [^{89}Zr]Zr-Df-LEM2/15 (2.6/3.4 fold) compared to both blocked LEM2/15 and IgG isotype control. This method established the specificity of the binding in vivo.

Targeted radionuclide therapy (TRT) uses radiolabelled antibodies that bind to targets on the surface of cancer cells for the specific delivery of ionizing radiation. Given that MT1-MMP is overexpressed in MDA-MB-231 cells [40] and our results demonstrate that the specific uptake of radiolabelled LEM2/15 is mediated by MT1-MMP binding, TRT against MT1-MMP may have broader applications in triple-negative breast cancer treatment. Here, we explored a TRT approach to treat MDA 231-BrM2–831 TNBC xenograft mice by employing ^{177}Lu-labelled LEM2/15 to specifically deliver therapeutic radiation to MT1-MMP-positive tumours. The tumour uptake of [^{177}Lu]Lu-DOTA-LEM2/15 was similar to that of [^{89}Zr]Zr-Df-LEM2/15 at 7 days post-injection (approximately 5–7%ID/g), indicating that tumour targeting was not affected by radionuclides or chelators. The [^{177}Lu]Lu-DOTA-LEM2/15-treated group of mice that received a 3-dose regimen showed superior tumour growth inhibition compared to those receiving a single dose of [^{177}Lu]Lu-DOTA-LEM2/15 or saline. The observed longer tumour doubling time in the treated group indicated effective intervention. Other biological marker in assessment of pharmacodynamics effects of tumour treatments is the direct detection of DNA damage; double-strand breaks (DSBs), which are considered the most relevant lesions to the DNA damage of ionizing radiation, may be detected on a molecular level by staining of the early DNA damage response marker, γH2AX. Of note, γH2AX has been shown to be a more sensitive as a marker of DSBs than the Comet assay, and has been recommended as a surrogate clinical marker of DNA damage [41]. Phosphorylation of histone H2AX is one of the earliest changes to occur at sites of DSBs damage, where it is thought to facilitate repair by maintaining structural changes in chromatin. The results of our study showed that treatment with the 3-dose regimen of [^{177}Lu]Lu-DOTA-LEM2/15 significantly increased the DSBs damage in tumour cells. Future work will focus on re-treatment with additional doses of [177Lu]Lu-DOTA-LEM2/15 to study absorbed radiation doses in tumour and normal tissues, aiming for a complete response in this TNBC xenograft model.

5. Conclusion

The current study shows that [^{89}Zr]Zr-Df-LEM2/15 and [^{177}Lu]Lu-DOTA-LEM2/15, which specifically target MT1-MMP, form an effective theranostic (imaging and therapeutic) pair and could serve as a potential therapeutic option for patients with MT1-MMP-positive TNBC. Further clinical evaluation and translation of this targeted theranostic approach may be relevant for TNBC patient stratification and management.

Funding

CRediT authorship contribution statement

Natalia Magro: Writing – review & editing, Writing – original draft, Visualization, Validation, Methodology, Investigation, Formal analysis, Data curation, Conceptualization. **Marta Oteo:** Writing – review & editing, Writing – original draft, Visualization, Validation, Supervision, Methodology, Investigation, Formal analysis, Data curation, Conceptualization. **Eduardo Romero:** Writing – review & editing, Writing – original draft, Methodology, Investigation. **Marta Ibáñez-Moragues:** Methodology, Investigation. **Victor Manuel Lujan:** Visualization, Investigation. **Laura Martínez:** Investigation. **Oscar Vela:** Visualization, Software. **Maria Elena López-Melero:** Methodology, Investigation. **Alicia G. Arroyo:** Writing – review & editing, Resources. **Guillermo Garaulet:** Resources, Methodology, Investigation, Formal analysis, Data curation. **Jorge Luis Martínez-Torrecuadrada:** Writing – review & editing, Supervision, Resources, Methodology, Conceptualization. **Francisca Mulero:** Writing – review & editing, Supervision, Resources, Funding acquisition, Conceptualization. **Miguel Angel Morcillo:** Writing – review & editing, Writing – original draft, Visualization, Validation, Supervision, Project administration, Methodology, Investigation, Funding acquisition, Formal analysis, Data curation, Conceptualization.

Declaration of competing interest

The authors declare that they have no known competing financial interests or personal relationships that could have appeared to influence the work reported in this paper.

Acknowledgements

Appendix A. Supplementary data

Supplementary data to this article can be found online at https://doi.org/10.1016/j.nucmedbio.2024.108930.

References

[1] Lehmann BD, Bauer JA, Chen X, Sanders ME, Chakravarthy AB, Shyr Y, et al. Identification of human triple-negative breast cancer subtypes and preclinical models for selection of targeted therapies. J Clin Invest 2011 Jul;121(7):2750–67. https://doi.org/10.1172/JCI45014.

[2] Rakha EA, El-Sayed ME, Reis-Filho J, Ellis IO. Patho-biological aspects of basal-like breast cancer. Breast Cancer Res Treat 2009 Feb;113(3):411–22. https://doi.org/10.1007/s10549-008-9952-1.

[3] Santa-Maria CA, Gradishar WJ. Changing treatment paradigms in metastatic breast cancer: lessons learned. JAMA Oncol 2015 Jul;1(4):528–34. quiz 549. https://doi.org/10.1001/jamaoncol.2015.1198.

[4] Foulkes WD, Smith IE, Reis-Filho JS. Triple-negative breast cancer. N Engl J Med 2010 Nov 11;363(20):1938–48. https://doi.org/10.1056/NEJMra1001389.

[5] Abramson VG, Lehmann BD, Ballinger TJ, Pietenpol JA. Subtyping of triple-negative breast cancer: implications for therapy. Cancer 2015 Jan 1;121(1):8–16. https://doi.org/10.1002/cncr.28914.

[6] Gerlinger M, Rowan AJ, Horswell S, Math M, Larkin J, Endesfelder D, et al. Intratumor heterogeneity and branched evolution revealed by multiregion sequencing. N Engl J Med 2012 Mar 8;366(10):883–92. https://doi.org/10.1056/NEJMoa1113205.

[7] Amir E, Miller N, Geddie W, Freedman O, Kassam F, Simmons C, et al. Prospective study evaluating the impact of tissue confirmation of metastatic disease in patients with breast cancer. J Clin Oncol 2012 Feb 20;30(6):587–92. https://doi.org/10.1200/JCO.2010.33.5232. Epub 2011 Nov 28. Erratum in: J Clin Oncol. 2016 Apr 1;34(10):1156.

[8] Choi H, Kim K. Theranostics for triple-negative breast cancer. Diagnostics (Basel) 2023 Jan 11;13(2):272. https://doi.org/10.3390/diagnostics13020272.

[9] Perentes JY, Kirkpatrick ND, Nagano S, Smith EY, Shaver CM, Sgroi D, et al. Cancer cell-associated MT1-MMP promotes blood vessel invasion and distant metastasis in

triple-negative mammary tumors. Cancer Res 2011 Jul 1;71(13):4527–38. https://doi.org/10.1158/0008-5472.CAN-10-4376.

[10] Zeng C, Lin M, Jin Y, Zhang J. Identification of key genes associated with brain metastasis from breast cancer: a bioinformatics analysis. Med Sci Monit 2022 Mar 17;28:e935071. https://doi.org/10.12659/MSM.935071.

[11] Li Y, Cai G, Yuan S, Jun Y, Li N, Wang L, et al. The overexpression membrane type 1 matrix metalloproteinase is associated with the progression and prognosis in breast cancer. Am J Transl Res 2015 Jan 15;7(1):120–7.

[12] Knapinska AM, Fields GB. The expanding role of MT1-MMP in cancer progression. Pharmaceuticals (Basel) 2019 May 20;12(2):77. https://doi.org/10.3390/ph12020077.

[13] Wei W, Rosenkrans ZT, Liu J, Huang G, Luo QY, Cai W. ImmunoPET: concept, design, and applications. Chem Rev 2020 Apr 22;120(8):3787–851. https://doi.org/10.1021/acs.chemrev.9b00738.

[14] Zhang Y, Hong H, Cai W. PET tracers based on Zirconium-89. Curr Radiopharm 2011 Apr;4(2):131–9. https://doi.org/10.2174/1874471011104020131.

[15] Dilworth JR, Pascu SI. The chemistry of PET imaging with zirconium-89. Chem Soc Rev 2018 Apr 23;47(8):2554–71. https://doi.org/10.1039/C7CS00014F.

[16] Jauw YWS, O'Donoghue JA, Zijlstra JM, Hoekstra OS, der Houven Menke-van, van Oordt CW, et al. 89Zr-immuno-PET: toward a noninvasive clinical tool to measure target engagement of therapeutic antibodies in vivo. J Nucl Med 2019 Dec;60(12):1825–32. https://doi.org/10.2967/jnumed.118.224568.

[17] Wijngaarden JE, Huisman MC, Pouw JEE, der Houven Menke-van, van Oordt CW, Jauw YWS, et al. Optimal imaging time points considering accuracy and precision of Patlak linearization for 89Zr-immuno-PET: a simulation study. EJNMMI Res 2022 Sep 5;12(1):54. https://doi.org/10.1186/s13550-022-00927-6.

[18] Parakh S, Lee ST, Gan HK, Scott AM. Radiolabelled antibodies for cancer imaging and therapy. Cancers (Basel) 2022 Mar 11;14(6):1454. https://doi.org/10.3390/cancers14061454.

[19] Gill MR, Falzone N, Du Y, Vallis KA. Targeted radionuclide therapy in combined-modality regimens. Lancet Oncol 2017 Jul;18(7):e414–23. https://doi.org/10.1016/S1470-2045(17)30379-0.

[20] Pouget JP, Navarro-Teulon I, Bardiès M, Chouin N, Cartron G, Pèlegrin A, et al. Clinical radioimmunotherapy—the role of radiobiology. Nat Rev Clin Oncol 2011 Nov 8;8(12):720–34. https://doi.org/10.1038/nrclinonc.2011.160.

[21] Kang L, Li C, Rosenkrans ZT, Huo N, Chen Z, Ehlerding EB, et al. CD38-targeted theranostics of lymphoma with 89Zr/177Lu-labelled daratumumab. Adv Sci (Weinh) 2021 Mar 15;8(10):2001879. https://doi.org/10.1002/advs.202001879.

[22] Perk LR, Vosjan MJ, Visser GW, Budde M, Jurek P, Kiefer GE, et al. p-Isothiocyanatobenzyl-desferrioxamine: a new bifunctional chelate for facile radiolabeling of monoclonal antibodies with zirconium-89 for immuno-PET imaging. Eur J Nucl Med Mol Imaging 2010 Feb;37(2):250–9. https://doi.org/10.1007/s00259-009-1263-1.

[23] Vosjan MJ, Perk LR, Visser GW, Budde M, Jurek P, Kiefer GE, et al. Conjugation and radiolabeling of monoclonal antibodies with zirconium-89 for PET imaging using the bifunctional chelate p-isothiocyanatobenzyl-desferrioxamine. Nat Protoc 2010 Apr;5(4):739–43. https://doi.org/10.1038/nprot.2010.13.

[24] Mulero F, Oteo M, Garaulet G, Magro N, Rebollo L, Medrano G, et al. Development of anti-membrane type 1-matrix metalloproteinase nanobodies as immunoPET probes for triple negative breast cancer imaging. Front Med (Lausanne) 2022 Nov 24;9:1058455. https://doi.org/10.3389/fmed.2022.1058455.

[25] Lindmo T, Boven E, Cuttitta F, Fedorko J, Bunn Jr PA. Determination of the immunoreactive fraction of radiolabeled monoclonal antibodies by linear extrapolation to binding at infinite antigen excess. J Immunol Methods 1984 Aug 3;72(1):77–89. https://doi.org/10.1016/0022-1759(84)90435-6.

[26] Logan J. Graphical analysis of PET data applied to reversible and irreversible tracers. Nucl Med Biol 2000 Oct;27(7):661–70. https://doi.org/10.1016/s0969-8051(00)00137-2.

[27] Wang Y, Pan D, Huang C, Chen B, Li M, Zhou S, et al. Dose escalation PET imaging for safety and effective therapy dose optimization of a bispecific antibody. MAbs 2020 Jan-Dec;12(1):1748322. https://doi.org/10.1080/19420862.2020.1748322.

[28] Jauw YWS, O'Donoghue JA, Zijlstra JM, Hoekstra OS, Menke-van der Houven van Oordt CW, Morschhauser F, et al. 89Zr-immuno-PET: toward a noninvasive clinical tool to measure target engagement of therapeutic antibodies in vivo. J Nucl Med 2019 Dec;60(12):1825–32. https://doi.org/10.2967/jnumed.118.224568.

[29] Ankhead P, Loughrey MB, Fernández JA, Dombrowski Y, McArt DG, Dunne PD, et al. QuPath: open source software for digital pathology image analysis. Sci Rep 2017 Dec 4;7(1):16878. https://doi.org/10.1038/s41598-017-17204-5.

[30] Udi Y, Grossman M, Solomonov I, Dym O, Rozenberg H, Moreno V, et al. Inhibition mechanism of membrane metalloprotease by an exosite-swiveling conformational antibody. Structure 2015 Jan 6;23(1):104–15. https://doi.org/10.1016/j.str.2014.10.012.

[31] Kwon MJ. Matrix metalloproteinases as therapeutic targets in breast cancer. Front Oncol 2023 Jan 19;12:1108695. https://doi.org/10.3389/fonc.2022.1108695.

[32] Gálvez BG, Matías-Román S, Albar JP, Sánchez-Madrid F, Arroyo AG. Membrane type 1-matrix metalloproteinase is activated during migration of human endothelial cells and modulates endothelial motility and matrix remodeling. J Biol Chem 2001 Oct 5;276(40):37491–500. https://doi.org/10.1074/jbc.M104094200.

[33] de Lucas AG, Schuhmacher AJ, Oteo M, Romero E, Cámara JA, de Martino A, et al. Targeting MT1-MMP as an immunoPET-based strategy for imaging gliomas. PloS One 2016 Jul 27;11(7):e0158634. https://doi.org/10.1371/journal.pone.0158634.

[34] Morcillo MÁ, García de Lucas Á, Oteo M, Romero E, Magro N, Ibáñez M, et al. MT1-MMP as a PET imaging biomarker for pancreas cancer management. Contrast Media Mol Imaging 2018 Aug 26;2018:8382148. https://doi.org/10.1155/2018/8382148.

[35] Bai JW, Qiu SQ, Zhang GJ. Molecular and functional imaging in cancer-targeted therapy: current applications and future directions. Signal Transduct Target Ther 2023 Feb 27;8(1):89. https://doi.org/10.1038/s41392-023-01366-y.

[36] Rong J, Haider A, Jeppesen TE, Josephson L, Liang SH. Radiochemistry for positron emission tomography. Nat Commun 2023 Jun 5;14(1):3257. https://doi.org/10.1038/s41467-023-36377-4.

[37] Kalaei Z, Manafi-Farid R, Rashidi B, Kiani FK, Zarei A, Fathi M, et al. The prognostic and therapeutic value and clinical implications of fibroblast activation protein-α as a novel biomarker in colorectal cancer. Cell Commun Signal 2023 Jun 14;21(1):139. https://doi.org/10.1186/s12964-023-01151-y.34.

[38] Truillet C, Oh HLJ, Yeo SP, Lee CY, Huynh LT, Wei J, et al. Imaging PD-L1 expression with immunoPET. Bioconjug Chem 2018 Jan 17;29(1):96–103. https://doi.org/10.1021/acs.bioconjchem.7b00631.

[39] Moek KL, Giesen D, Kok IC, de Groot DJA, Jalving M, Fehrmann RSN, et al. Theranostics using antibodies and antibody-related therapeutics. J Nucl Med 2017 Sep;58(Suppl. 2):83S–90S. https://doi.org/10.2967/jnumed.116.186940.

[40] Ling B, Watt K, Banerjee S, Newsted D, Truesdell P, Adams J, et al. A novel immunotherapy targeting MMP-14 limits hypoxia, immune suppression and metastasis in triple-negative breast cancer models. Oncotarget 2017 May 9;8(35):58372–85. https://doi.org/10.18632/oncotarget.17702.

[41] Wu J, Clingen PH, Spanswick VJ, Mellinas-Gomez M, Meyer T, Puzanov I, et al. γ-H2AX foci formation as a pharmacodynamic marker of DNA damage produced by DNA cross-linking agents: results from 2 phase I clinical trials of SJG-136 (SG2000). Clin Cancer Res 2013 Feb 1;19(3):721–30. https://doi.org/10.1158/1078-0432.CCR-12-2529.